Biophysical Journal
Article

Biophysical Society

Properties of a tardigrade desiccation-tolerance protein aerogel

Jonathan Eicher,[1] Brent O. Hutcheson,[1] and Gary J. Pielak[1,2,3,4,*]
[1]Department of Chemistry, University of North Carolina, Chapel Hill, North Carolina; [2]Department of Biochemistry and Biophysics, University of North Carolina, Chapel Hill, North Carolina; [3]Lineberger Comprehensive Cancer Center, University of North Carolina, Chapel Hill, North Carolina; and [4]Integrative Program for Biological and Genome Sciences, University of North Carolina, Chapel Hill, North Carolina

ABSTRACT Lyophilization is promising for tackling degradation during the drying and storage of protein-based drugs. Tardigrade cytosolically abundant heat soluble (CAHS) proteins are necessary and sufficient for desiccation-tolerance in vivo and protein protection in vitro. Hydrated CAHS proteins form coiled-coil-based fine-stranded, cold-setting hydrogels, but the dried protein remains largely uncharacterized. Here, we show that dried CAHS D gels (i.e., aerogels) retain the structural units of their hydrogels, but the details depend on prelyophilization CAHS concentrations. Low concentration samples (<10 g/L) form thin (<0.2 μm) tangled fibrils lacking regular structure on the micron scale. Upon increasing the concentration, the fibers thicken and form slabs comprising the walls of the aerogel pores. These changes in morphology are associated with a loss in disorder and an increase in large β sheets and a decrease in α helices and random coils. This disorder-to-order transition is also seen in hydrated gels as a function of concentration. These results suggest a mechanism for pore formation and indicate that using CAHS proteins as excipients will require attention to initial conditions because the starting concentration impacts the lyophilized product.

SIGNIFICANCE Tardigrade desiccation tolerance proteins are important both fundamentally and practically. Fundamentally important because these strange, disordered, gel-forming proteins allow these amazing animals, often called water bears, to survive decades of desiccation. Practically important because it might be possible to use these proteins to preserve protein-based drugs, vaccines, and industrial enzymes without the need for a cold chain.

INTRODUCTION

The production, storage, and transport of protein-based pharmaceutical drugs requires careful consideration of environmental conditions because proteins are unstable (1). Strategies to combat degradation focus on reducing the temperature (2). This requirement for uninterrupted low temperature, referred to as the cold chain, makes storage and distribution both difficult and costly (3). The barrier to degradation can be increased by lyophilization, but this process is often damaging (4).

As defined by Gokarn et al. (5), "Excipients are additives that are included in a formulation, because they either impart or enhance the stability, delivery, and manufacturability of a drug product." Adding excipients can minimize damage, but excipients are often client specific so new ones are always in demand. Cytosolically abundant heat soluble (CAHS) proteins from tardigrades (6) are a potential source of novel excipients (7–12). These proteins form phase-separated droplets in vivo (13) and flexible fine-stranded fibrous gels at concentrations of 20 g/L or greater in vitro (14). The mechanism of the proteins' ability to protect against desiccation damage requires understanding both its hydrated and dried structures. The fibers in CAHS gels comprise coiled-coils that form higher order gelation-competent oligomers (14,15). Creation of terminal intermolecular β-sheets drives gelation by forming junctions between fibers. The gel is melted by heat, which destroys these secondary structures, or by dilution, which mitigates intermolecular interactions (15).

What is the structure of dry CAHS protein assemblies? Air drying CAHS gels promotes fibrillation through α-helix formation (compared to dilute solutions of the protein) (13). Drying cells expressing CAHS protein increases stiffness, suggesting maintenance of the gel matrix structure in the absence of water (16). In tardigrades, this

Submitted February 9, 2023, and accepted for publication May 3, 2023.
*Correspondence: gary_pielak@unc.edu
Editor: Ronald Koder.
https://doi.org/10.1016/j.bpj.2023.05.002

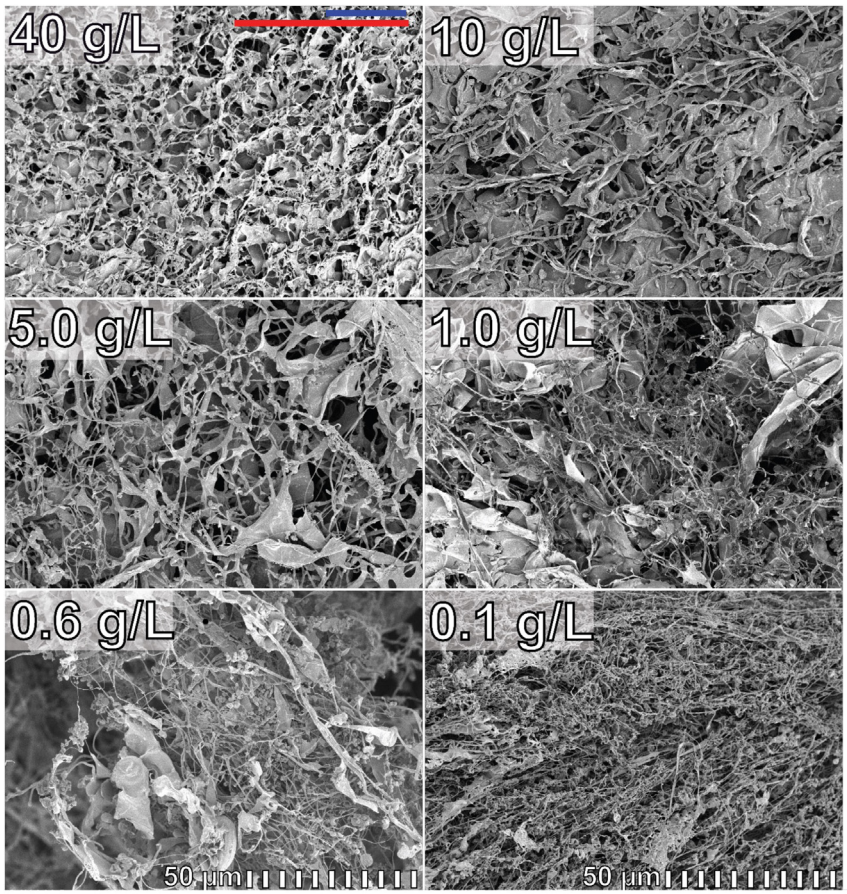

FIGURE 1 Scanning electron micrographs of lyophilized CAHS D made from liquid samples of the indicated CAHS D concentrations. Blue and red lines in the top left panel are estimated end-to-end lengths of 5000 CAHS D proteins in collapsed (*blue*) or highly denatured (*red*) forms (27,28). To see this figure in color, go online.

structure becomes apparent through ultrastructural analysis of transmission electron microscopy images (17).

Here, we examine how the initial concentration of a wet CAHS protein (CAHS D) (7–10,18) affects its structure after lyophilization (i.e., the aerogel) by using scanning electron microscopy (SEM) and attenuated total reflectance Fourier transform infrared spectroscopy (ATR-FTIR). SEM allows direct observation of micrometer- and nanometer-scale features, providing context to the secondary structure of CAHS D aerogels derived from FTIR spectra of the amide I (1600–1700 cm^{-1}) region.

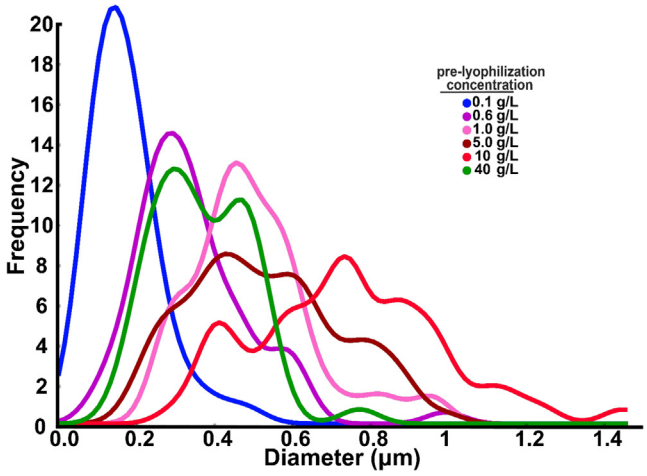

FIGURE 2 Fitted distributions of CAHS D fiber diameters (bin size, 0.05 μm; kernel distribution). To see this figure in color, go online.

Analysis of FTIR spectra benefits from dimensionality reduction (19). Each spectrum includes a range of wavenumbers, yet a set of spectra related by, for instance, concentration, may describe only a handful of distinct states. Principal component analysis (PCA) linearly projects high-dimensional data into a low-dimensional space of principal components. The relationship between spectral features and a principal component is scored using a loading plot, which generates a single value for each spectrum. The scores provide discrimination of complex transitions, and loading plots identify features relevant to the transitions (20).

MATERIALS AND METHODS

Sample preparation

Protein expression and purification were performed as described (15). Samples were prepared by dissolving purified CAHS D in buffer (13.7 mM NaCl, 0.27 mM KCl, 0.8 mM Na_2HPO_4, 0.2 mM KH_2PO_4 [pH 7.4]). Dissolution was accomplished by sequential heating on a 42°C heat block with

flicking and pulse centrifugation on a tabletop centrifuge. The concentration was determined using a Pierce Coomassie Plus assay with a bovine serum albumin standard (Sigma Aldrich, St. Louis, MO, USA) in 96-well plates (21). Aliquots were prepared such that samples contained 1 mg of protein. Samples were then flash frozen in an ethanol-CO_2 (s) bath for 10 min, followed by lyophilization (Labconco FreeZone 1 Liter Benchtop Freeze Dry System, Kansas City, MO, USA).

ATR-FTIR

Absorbance spectra were recorded on a dry-air purged BioTools Prota-3S spectrophotometer with an Hg Cd Te detector and a ZnSe-diamond ATR. Spectra comprising 100 scans were acquired from 805 to 5500 cm^{-1} with 4 cm^{-1} resolution, as defined by the instrument. The dried protein was placed on the stage and compressed to ensure flush contact with the crystal. Background and vapor spectra were subtracted using Prota3s software (BioTools, Jupiter, FL, USA). The spectra were processed with an Orange Datamining workflow using a rubberband baseline and vector normalization. Difference spectra were generated by subtracting the average of spectra from 50 g/L samples. The second derivative spectra were calculated with a Savitsky-Golay filter with a window size of 9 and a second-order polynomial. The peaks were used to fit Voigt profiles using nonlinear least-squares regression. Peak area was used to calculate the percentage of each secondary structure, excluding the aromatics and amide II contributions. PCA was performed on the amide I and II (1500–1700 cm^{-1}) regions of the processed spectra.

SEM

Images were acquired on a Hitachi S-4700 (Tokyo, Japan) field emission microscope. Double-stick carbon tape was used to fix the protein to an Al SEM sample holder. The samples were coated with a layer of 7.5 nm Au-Pd alloy. Operating conditions comprised normal mode, 2 kV accelerating voltage, 10 μA beam current, and a working distance near 12 mm. Diameters were estimated using Fiji's measurement tool (22).

RESULTS

CAHS D samples have been studied with FTIR (13,15) but not with SEM and not as function of concentration. Here, we use ATR-FTIR and SEM to examine the effect of initial CAHS D concentration on dry CAHS D structure. When prepared from solutions of 10 g/L CAHS D or less, the dried samples are soft and bunch into thin irregularly shaped straws. At intermediate concentrations, 10–20 g/L, where the hydrated protein forms gels (15), the aerogels are like cotton candy, filling about the same volume as the hydrogels. Postgelation (>20 g/L), the samples are similar to puffed rice.

SEM

Comparing the macroscopic aerogels—straws, cotton candy, puffed rice, which retain the dimensions of the hydrogel—with SEM images (Fig. 1) gives context to their properties. CAHS D gels lyophilized at various concentrations give rise to several morphologies, including nodules, slabs, and fibers. Nodules are common at lower concentrations, but their frequency drops at higher concentrations. Fibrils are present at all concentrations whereas knotted tangles appear at initial concentrations <1.0 g/L. Slabs appear as early as 0.6 g/L, maturing to more regular structures with increasing initial CAHS D concentration.

A variety of asymmetric nodule structures appear at lower concentrations (Fig. 1). These nodules flocculate, forming clusters that do not appear connected to a larger overall structure. As the initial CAHS D concentration increases, the frequency of nodules decreases, with the first decrease occurring at 1.0 g/L. At this concentration, nodules begin to appear at strand ends, with nodule size proportional to strand size. By 40 g/L there are no easily identifiable nodules.

A regular porous aerogel structure is apparent in samples prepared from an initial concentration of 40 g/L. SEM reveals ~8 μm pores, but more precise dimensions are difficult to determine because sample preparation flattens the surface. Slabs are the prevalent feature in the 40 g/L sample,

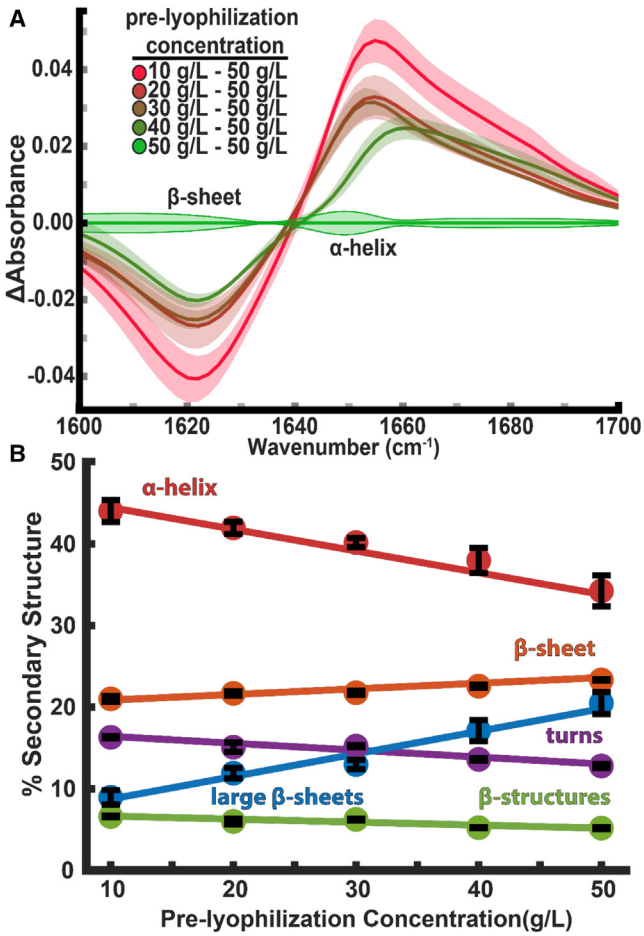

FIGURE 3 Triplicated difference spectra of lyophilized CAHS D (ranges are shaded). The averaged spectrum of the highest prelyophilized concentration (50 g/L) is subtracted from each averaged spectrum. (*A*) Secondary structure of lyophilized CAHS D with respect to prelyophilization concentration, error bars are the standard deviation of the mean. (*B*) The lines are aids to the eye and of no theoretical significance. Peak assignments: α helix, 1650 ± 0.6 cm^{-1}; β sheet, 1634 ± 0.9 cm^{-1}; turns, 1670 ± 0.4 cm^{-1}; large β sheets, 1620 ± 0.7 cm^{-1}; β structures, 1686 ± 0.4 cm^{-1} (25,26). To see this figure in color, go online.

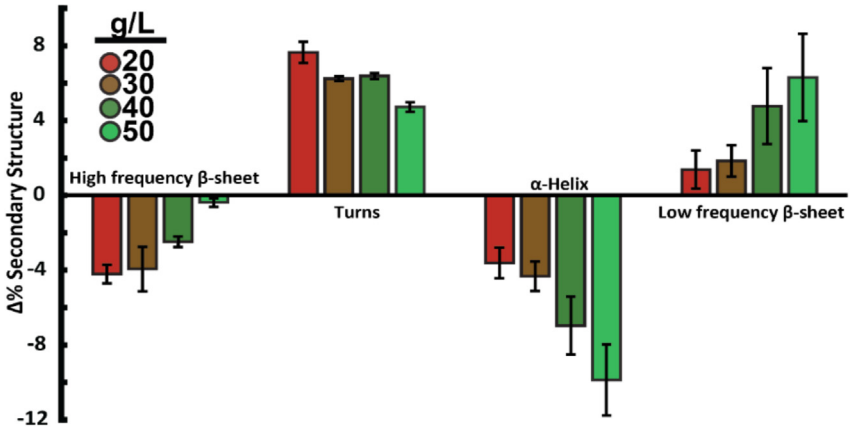

FIGURE 4 Percent secondary structure in lyophilized samples minus percent secondary structure in the hydrogels from which the dry samples are made (15). Positive values indicate a gain of structure in the lyophilized state. Uncertainties in the differences are propagated from the standard deviations (from triplicated spectra of independent samples) of the values for the dry and wet samples. To see this figure in color, go online.

like they are at 10 g/L, but at the higher initial concentrations the slabs align and form the flat structures, many of which are perpendicular to the plane (Fig. S1) making them more challenging to see.

Fibril diameter is quantifiable even at the lowest initial CAHS D concentration, 0.1 g/L (Fig. S2). These fibers have a mean diameter of 0.17 μm. The diameter increases with initial concentration, with fibers from the 10 g/L sample reaching a mean of 0.74 μm. However, at an initial CAHS D concentration of 40 g/L, the mean fibril width drops to 0.37 μm.

We studied the distribution of diameters (Fig. 2). Fibers formed at the lowest initial CAHS D concentration give rise to a single distribution at $\sim$0.1 μm. At 0.6 g/L there is one major peak at $\sim$0.3 μm and a shoulder at $\sim$0.6 μm. At 1.0 g/L the trend is inverted with a major peak at $\sim$0.5 μm and a shoulder at $\sim$0.3 μm. At 5.0 g/L, the average moves to larger diameters and the distribution becomes complex. The 10 g/L sample follows the same pattern as the 5.0 g/L sample, shifting toward a higher average diameter. The 40 g/L sample breaks this trend, with two nearly identical major peaks at sizes reminiscent of those from the 0.6 and 1.0 g/L samples.

ATR-FTIR spectroscopy

We acquired spectra of CAHS D samples dried from a variety of initial concentrations (Fig. S3). FTIR provides ensemble averaged information about molecular oscillators. Ensemble averaging is important because of the heterogeneity observed in the SEM images, especially those from samples prepared at low initial CAHS D concentrations (Fig. 1).

FTIR spectra of wet CAHS D samples show that coiled-coil fibrils gel via intermolecular interactions between terminal β-sheets (15). Spectra of dried samples prepared at pregelation concentrations (<10 g/L) to postgelation concentrations (50 g/L) (15) show compensation between high- and low-wavenumber features similar to those observed with hydrogel melting, with a downshifted isosbestic point, from $\sim$1655 cm^{-1} in wet samples (15) to $\sim$1640 cm^{-1} in dry samples (Fig. 3 *A*).

The fitted bands identify (Fig. 3 *B*) a variety of structures in the dry samples, but α-helices predominate. There is little change in secondary structure for samples prepared at concentrations <10 g/L (Fig. S4). As the initial CAHS D concentration increases past 10 g/L the helix and turn content drops, with a compensatory increase in large β-sheets. This change reflects an increase in the number of intermolecular interactions (23), which coincides with slab formation in the SEM images (Fig. 1).

PCA reveals the highest variance in the amide I and II bands (1500–1700 cm^{-1}) (Fig. S5) (20). PC1 captures a dependence on the concentration of CAHS D used to prepare aerogels (Fig. S6). The positive feature at 1550 cm^{-1} in the loading plot (Fig. S7) indicates a positive correlation between gelation/aerogel formation and α-helix (24,25). The apparent decrease in fitted α-helix/random coil content may arise from convolution with a random coil band that appears as a broad feature at 1645 cm^{-1} (24). An increase in large β-sheets in the dry state with increasing initial concentration is indicated by the strong 1620 cm^{-1} band (26).

CAHS D aerogels have a higher proportion of turns and low-frequency β-structures compared with the hydrogels from which they form (Fig. 4). The low-frequency β-structures could correspond to the slabs in the SEM images (Fig. 1). This transition from flexible strands to ordered slabs would match the decrease in turns with increasing concentration as flexible terminal domains (14) settle into intermolecular β-sheet junctions (15). The convolution of the α-helical and random coil band described above could then explain the relative reduction in band area as a part of this disorder-to-order transition.

DISCUSSION

It is of interest to compare the features in the micrographs (Fig. 1) to the dimensions of CAHS D assuming its hydrodynamic radius reflects a globular or fully extended protein (27,28). The fibril diameter, at its smallest, comprises 10 globular or 20 extended CAHS D proteins (Fig. 1). As the fibers thicken, that number reaches toward 50–100 proteins, while the pores are thousands of CAHS D proteins wide.

These scales show the huge number of proteins involved in forming the hydrogels and aerogels.

The transition from thin, flexible, knotted fibers to ordered slabs that form the pore walls correlates (Fig. 1) with gelation, which occurs above 10 g/L (15). The fibers thicken (Fig. S2) up to the concentration of 10 g/L. The diameter of the major species peaks at 0.6 μm at 1.0 g/L (Fig. 2). Further increases in initial concentration give larger diameters but a more diffuse number of species. At 40 g/L the distribution settles back to something like the simpler distributions of 0.6 and 1.0 g/L. The similarity between the 0.6–1.0 and the 40 g/L samples suggests that, at postgelation concentrations, fibers >0.6 μm are less stable. In the micrographs (Fig. 1), starting at 5.0 g/L there is a sharp rise in slab formation, a feature uncommon at lower concentrations. While the slabs are connected by fibers, they show little of the organization of regular pore structure until 40 g/L. The less-structured distribution and appearance of unordered slabs likely result from the same mechanism, which we propose involves stacking of fibers into slabs. At low concentrations, the slabs are unable to bind one another fully because of the greater distances in solution. Once a full gel forms, fibers above the threshold of 0.6 μm are more likely to interact with a nearby slab than with water, explaining why mostly smaller fibers are present in the 40 g/L samples.

FTIR data show that as the initial CAHS D concentration increases, random coil and turn content drops, with a compensatory increase in large β-sheets (Figs. 3 and 4). This change is interpreted as an increase in the number of intermolecular interactions (23), which is manifested as slab formation in SEM images (Fig. 1). As described by Lomont et al. (29), the modest change in the 1634 cm^{-1} β-sheet in the dried state indicates that the smaller 3–4 strand sheets are not favored upon drying. This change in β-structure is in contrast to the hydrated samples, which lack a significant 1620 cm^{-1} band, implying the hydrogel is formed via these small β-sheets (15). At lower concentrations there is no change in large β-sheet content indicating a lack of importance in pregelling samples (Fig. S4). Aerogels retain the same high- to low-frequency β-sheet transition as hydrogels upon increasing concentration (15), supplemented by decreases in α-helices and turns (Fig. 4). This high-to-low transition suggests that, upon drying, the disordered end regions of CAHS D stabilize the pore structures through zipper-like interactions forming large β-sheets.

CONCLUSIONS

The most important message is that the structure of dry CAHS D depends on its initial concentration. That is, the starting concentration of CAHS D, and probably other tardigrade desiccation-tolerance proteins, must be borne in mind when assessing protection. The observation is important because protein structure on the micrometer scale is not often linked to concentration when experiments are performed in solution. Some structures from the hydrogels are retained upon lyophilization, as inferred in vivo (16). The transition from helix/random coil to β-sheets upon increasing the initial concentration coincides with the transition from thin fibrils to thicker fibrils in the micrographs, eventually resulting in ordered slabs (Figs. 1, 3, and 4). The transition occurs independently of the fiber size (Fig. 2), implying that fibers with diameters greater than ~0.6 μm become part of the walls of the aerogel pores at higher concentrations. Upon drying, the pore structure is stabilized by the formation of large β sheets on the edge of the slabs via a disorder-to-order transition (Fig. 4). Our observations describe the structural features of lyophilized CAHS D and suggest that the pores are important for protecting macromolecules during drying, which may inform the use of these proteins as excipients.

SUPPORTING MATERIAL

Supporting material can be found online at https://doi.org/10.1016/j.bpj.2023.05.002.

AUTHOR CONTRIBUTIONS

J.E. and B.O.H. performed the research, contributed analytical tools, and analyzed data. J.E., B.O.H., and G.J.P. analyzed data and wrote the paper.

ACKNOWLEDGMENTS

We thank the Pielak lab for helpful discussions, Amar Kumbhar for help with SEM, and Elizabeth Pielak for comments on the manuscript. This work was performed in part at the Chapel Hill Analytical and Nanofabrication Laboratory, a member of the North Carolina Research Triangle Nanotechnology Network, which is supported by the National Science Foundation (ECCS-1542015) as part of the National Nanotechnology Coordinated Infrastructure. This work was supported by the National Science Foundation (CHE-2203505) and the National Institutes of Health (R01GM127291) to G.J.P. We thank the National Institutes of Health for training support (T32GM008570).

DECLARATION OF INTERESTS

The authors declare no competing interests.

REFERENCES

1. Krause, M. E., and E. Sahin. 2019. Chemical and physical instabilities in manufacturing and storage of therapeutic proteins. *Curr. Opin. Biotechnol.* 60:159–167.
2. Muralidhara, B. K., and M. Wong. 2020. Critical considerations in the formulation development of parenteral biologic drugs. *Drug Discov. Today.* 25:574–581.
3. Pambudi, N. A., A. Sarifudin, …, R. Romadhon. 2022. Vaccine cold chain management and cold storage technology to address the challenges of vaccination programs. *Energy Rep.* 8:955–972.

4. Moorthy, B. S., L. K. Iyer, …, E. M. Topp. 2015. Characterizing protein structure, dynamics and conformation in lyophilized solids. *Curr. Pharm. Des.* 21:5845–5853.
5. Gokarn, Y. R., A. Kosky, …, R. L. Remmele, Jr. 2006. *In* Excipients for Protein Drugs. Excipient Development for Pharmaceutical, Biotechnological, and Drug Delivery Sytstems, A. Katdare and M. V. Chaubal, eds Informa Healthcare, pp. 291–331.
6. Yamaguchi, A., S. Tanaka, …, T. Kunieda. 2012. Two novel heat-soluble protein families abundantly expressed in an anhydrobiotic tardigrade. *PLoS One.* 7, e44209.
7. Boothby, T. C., H. Tapia, …, B. Goldstein. 2017. Tardigrades use intrinsically disordered proteins to survive desiccation. *Mol. Cell.* 65:975–984.e5.
8. Piszkiewicz, S., K. H. Gunn, …, G. J. Pielak. 2019. Protecting activity of desiccated enzymes. *Protein Sci.* 28:941–951.
9. Esterly, H. J., C. J. Crilly, …, B. E. Christian. 2020. Toxicity and immunogenicity of a tardigrade cytosolic abundant heat soluble protein in mice. *Front. Pharmacol.* 11, 565969.
10. Crilly, C. J., J. A. Brom, …, G. J. Pielak. 2022. Protection by desiccation-tolerance proteins probed at the residue level. *Protein Sci.* 31:396–406.
11. Nguyen, K., S. Kc, …, T. C. Boothby. 2022. Trehalose and tardigrade CAHS proteins work synergistically to promote desiccation tolerance. *Commun. Biol.* 5:1046.
12. Packebush, M. H., S. Sanchez-Martinez, …, T. C. Boothby. 2023. Natural and engineered mediators of desiccation tolerance stabilize human blood clotting factor viii in a dry state. *Sci. Rep.* 13:4542.
13. Yagi-Utsumi, M., K. Aoki, …, K. Kato. 2021. Desiccation-induced fibrous condensation of CAHS protein from an anhydrobiotic tardigrade. *Sci. Rep.* 11, 21328.
14. Malki, A., J.-M. Teulon, …, M. Blackledge. 2022. Intrinsically disordered tardigrade proteins self-assemble into fibrous gels in response to environmental stress. *Angew. Chem., Int. Ed.* 61, e202109961.
15. Eicher, J. E., J. A. Brom, …, G. J. Pielak. 2022. Secondary structure and stability of a gel-forming tardigrade desiccation-tolerance protein. *Protein Sci.* 31:e4495.
16. Tanaka, A., T. Nakano, …, T. Kunieda. 2022. Stress-dependent cell stiffening by tardigrade tolerance proteins that reversibly form a filamentous network and gel. *PLoS Biol.* 20, e3001780.
17. Richaud, M., E. Le Goff, …, S. Galas. 2020. Ultrastructural analysis of the dehydrated tardigrade Hypsibius exemplaris unveils an anhydrobiotic-specific architecture. *Sci. Rep.* 10:4324.
18. Hesgrove, C., and T. C. Boothby. 2020. The biology of tardigrade disordered proteins in extreme stress tolerance. *Cell Commun. Signal.* 18:178.
19. Wilcox, K. 2014. Using Regression Analyses for the Determination of Protein Structure from FTIR Spectra. University of Manchester.
20. Christophe, B. Y. C. 2012. *In* PCA: The Basic Building Block of Chemometrics. Analytical Chemistry, S. K. Ira, ed IntechOpen.
21. Bradford, M. M. 1976. A rapid and sensitive method for the quantitation of microgram quantities of protein utilizing the principle of protein dye binding. *Anal. Biochem.* 72:248–254.
22. Schindelin, J., I. Arganda-Carreras, …, A. Cardona. 2012. Fiji: an open-source platform for biological-image analysis. *Nat. Methods.* 9:676–682.
23. Heimburg, T., J. Schünemann, …, N. Geisler. 1999. FTIR-spectroscopy of multistranded coiled coil proteins. *Biochemistry.* 38:12727–12734.
24. De Meutter, J., and E. Goormaghtigh. 2021. Amino acid side chain contribution to protein FTIR spectra: impact on secondary structure evaluation. *Eur. Biophys. J.* 50:641–651.
25. Sadat, A., and I. J. Joye. 2020. Peak fitting applied to Fourier transform infrared and Raman spectroscopic analysis of proteins. *Appl. Sci.* 10:5918.
26. Wilkins, D. K., C. M. Dobson, and M. Groß. 2000. Biophysical studies of the development of amyloid fibrils from a peptide fragment of cold shock protein B. *Eur. J. Biochem.* 267:2609–2616.
27. Wilkins, D. K., S. B. Grimshaw, …, L. J. Smith. 1999. Hydrodynamic radii of native and denatured proteins measured by pulsed field gradient NMR techniques. *Biochemistry.* 38:16424–16431.
28. Morar, A. S., A. Olteanu, …, G. J. Pielak. 2001. Solvent-induced collapse of α-synuclein and acid denatured cytochrome *c*. *Protein Sci.* 10:2195–2199.
29. Lomont, J. P., J. S. Ostrander, …, M. T. Zanni. 2017. Not all β-sheets are the same: amyloid infrared spectra, transition dipole strengths, and couplings investigated by 2D IR spectroscopy. *J. Phys. Chem. B.* 121:8935–8945.